Compliant joint to reduce docking loads between CubeSats

Francesco Branz[a,*], Alessandro Francesconi[a]

[a] *Department of Industrial Engineering, University of Padova, via Venezia 1, 35131 Padova, Italy*

Abstract

This paper presents the design, modelling and experimental verification of a damping joint for application to miniature space docking mechanisms. The joint design is based on deformable elastomeric elements, thus avoiding any sliding or contact between moving components. Numerical FEM simulations have been conducted in order to quantify the joint mechanical characteristics (rigidity and damping coefficient) as a function of the main design parameters (geometry, material, assembly). The obtained parametric relations provide an estimate of the joint characteristics based on the selected design. An equivalent visco–elastic model is developed and implemented in dynamic simulations. The results of the experimental evaluation of the joint design provide a validation of the developed models and prove the advantage of adopting damping joints in docking applications between small satellites, like reduced contact loads and enhanced damping.

Keywords: Passive compliant joint, Damping joint, CubeSat docking

1. Introduction

The space industry is experiencing a revolution in the way missions are implemented, with a strong trend towards the reduction of the size and complexity of satellites [1]. The goal is to reduce the cost of space systems through the development of mission architectures that foster the adoption of small satellites as enabled by the miniaturization of key technologies. Mission objectives are more often pursued by means of multiple compact vehicles, possibly organized in constellations, rather than large bulky platforms. The critical technologies required to enable this paradigm shift and to maximise its advantages are those related to the management of large constellation of small satellites, namely advanced propulsion systems, high–throughput communication systems and In-Orbit Servicing enabling technologies [2]. The latter include docking systems, which are often required to realize mission scenarios with physical interaction between multiple satellites.

A number of miniature docking mechanism designs are available in the literature, implementing a variety of different design solutions including the classical probe–drogue configuration [3, 4, 5], symmetric designs either flat [6, 7] or gripper–like [8, 9], magnetic systems [10]. The diversity of the proposed solutions comes from the unique challenges that the docking between small satellites poses to the involved systems. Often executed in autonomy, the docking manoeuvre requires the capability to accurately determine and control the relative pose between the two vehicles, the robustness to uncertain parameters and the minimization of safety risks.

The management of contact loads is a key aspect in the development of docking scenarios, but it is rarely discussed in the literature. Strong impulsive forces and torques at contact may be the cause of undesired dynamics (e.g., rebounds) or damages to either satellite. Contact loads depend on the final relative velocity and angular rate, and, therefore, strong requirements need to be posed to the design of the satellite Guidance, Navigation and Control (GNC) and propulsion systems. The adoption of docking interfaces capable to mitigate the effects of hard contacts would increase the overall robustness to uncertainties (e.g., mass, moments of inertia, center of mass position) or malfunctions, adding to the mission safety. This work proposes to equip small–satellite docking mechanisms with passive damping joints in order to reduce the loads exchanged at contact and to improve the dissipation of relative kinetic energy after docking. A specific joint design is presented, but the main results have a general value.

The remainder of the paper is organized as follows: Sec. 2 describes the damping joint design, Sec. 3 presents the model developed for the assessment of the joint dynamic performance, Sec. 4 discusses the numerical simulations (FEM and dynamic) executed on the joint model, Sec. 5 reports on the experimental validation of the joint prototype and Sec. 6 draws the conclusions.

2. Damping joint design

The proposed damping joint is based on a frictionless and wearless solid–state design that allows for 6 DoFs. Figure 9 depicts a prototype of the joint. The relative

*Corresponding author
Email address: francesco.branz@unipd.it (Francesco Branz)

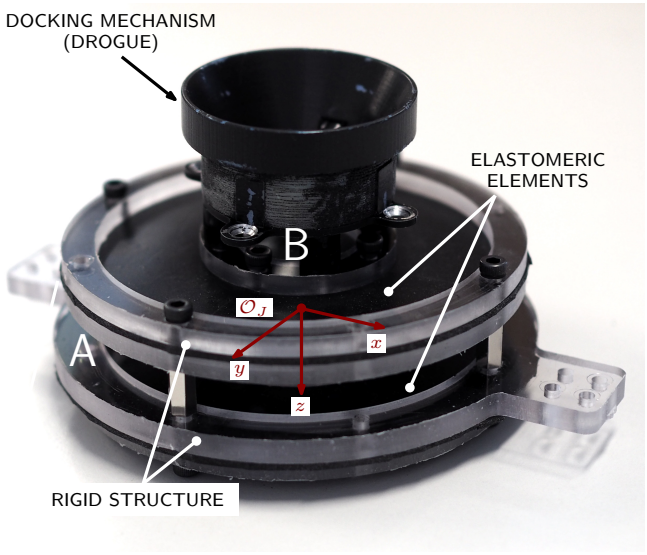

Figure 1: Picture of the damping joint prototype tested during the experimental campaign.

motion between the stator (A) and the mobile part (B) is allowed by deformable elastomeric elements. The joint has an axial–symmetric geometry. It is composed by two rigid structures and a set of two deformable elements, which are ring–shaped components manufactured from a rubber sheet. Figure 2 presents a schematic view of the damping joint, whose circular geometry can easily fit a probe–drogue docking mechanism, like the one described in [5]. The joint frame of reference is shown: the Z axis is the symmetry axis of the device, the X and Y axes are radial, horizontal and vertical respectively. The joint can deform along all DoFs (three translations and three rotations) and the variables that describe the motion of B with respect to A are the following:

$$\boldsymbol{x} = \{x, y, z, \phi, \vartheta, \psi\}^T \tag{1}$$

The geometry of the deformable section of the device is defined by four parameters, shown in Fig. 2: the external diameter, d_e, and internal diameter, d_i, of the rubber disks, the axial distance, b, between the midplanes of the rubber elements, and their thickness, t. Through a proper sizing of these quantities, it is possible to obtain different joint designs characterized by different values of rigidities and, therefore, dynamic response of the device.

3. Joint dynamic model

Elastomers show a highly non–linear visco–elastic behaviour affected by hysteresis and damage phenomena. Complex and computationally inefficient constitutive models are required to accurately describe the dynamic behaviour of elastomeric components. Nevertheless, the majority of these non–linear and time–dependent phenomena are relevant only when large deformations occur over long

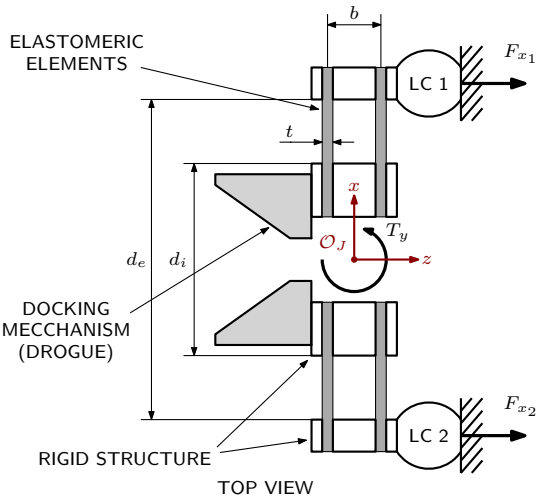

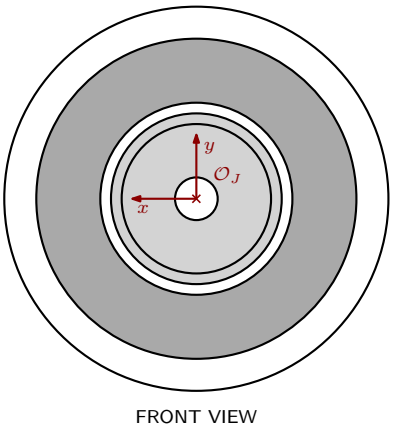

Figure 2: Schematic views of the proposed damping joint design showing reference frame, main geometric parameters, load cells position and measured forces.

time scales. In the presented analysis a simplified linear visco–elastic model is adopted, since the rubber elements of the designed joint undergo only small deformations at rather high frequencies (1–100 Hz) when applied to the damping of docking forces.

All the DoFs of the joint are allowed by the deformation of the same rubber elements, hence the different motion modes are, in principle, coupled. The dynamics of each DoF is influenced, to some extend, by the deformation of the joint along the other DoFs. Nevertheless, in the small deformations hypothesis, the coupling effects are generally negligible and the joint deformation model adopted is decoupled.

The simplified model is an equivalent linear mass–spring–damper model, whose parameters are tuned to match the non–linear dynamics of the joint. In the considered configuration, the joint stator A is fixed (not moving) and the joint mobile part B is attached to a docked vehicle (e.g., CubeSat – C) with which constitutes the moving object (B+C) in the model. A simplified graphic representation of the model is shown in Fig. 3. The inertial properties of

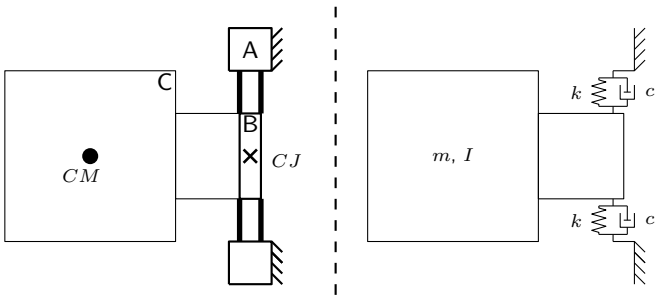

Figure 3: Schematic representation of the main bodies composing the system and of the linear multi–DoF visco–elastic model adopted.

the system are:

$$\boldsymbol{m} = \left\{ m, m, m, I_x^{(CJ)}, I_y^{(CJ)}, I_z^{(CJ)} \right\}^T \tag{2}$$

where m is the mass of the moving object (B+C), and $I_x^{(CJ)}$, $I_y^{(CJ)}$ and $I_z^{(CJ)}$ are its moments of inertia computed with respect to the joint center CJ.

Joint rigidities and damping coefficients are defined for each DoF:

$$\begin{aligned} \boldsymbol{k} &= \{k_x, k_y, k_z, k_\phi, k_\vartheta, k_\psi\}^T \\ \boldsymbol{c} &= \{c_x, c_y, c_z, c_\phi, c_\vartheta, c_\psi\}^T \end{aligned} \tag{3}$$

allowing to compute the elastic and viscous forces generated by the joint:

$$\begin{aligned} \boldsymbol{F_k} &= \{k_x x, k_y y, k_z z, k_\phi \phi, k_\vartheta \vartheta, k_\psi \psi\}^T \\ \boldsymbol{F_c} &= \{c_x \dot{x}, c_y \dot{y}, c_z \dot{z}, c_\phi \dot{\phi}, c_\vartheta \dot{\vartheta}, c_\psi \dot{\psi}\}^T \end{aligned} \tag{4}$$

The joint rigidity is a function of the material elastic modulus (Young's modulus). Elastomers are often classified based on their hardness, which is measured as the depth of the indentation in the material caused by a tool pressed on the material with a given force. Among other scales, Shore A is used to test relatively soft materials with an indenter shaped as a truncated cone. An approximated relation exists between the Shore A hardness, H, and the Young's modulus, E (in MPa):

$$E = \left[\frac{\mathrm{erf}^{-1}\left(\frac{H}{100}\right)}{3.186 \times 10^{-4}} \right]^2 \times 10^{-6} \tag{5}$$

where $\mathrm{erf}(\cdot)$ is the Gauss error function:

$$\mathrm{erf}(z) = \frac{2}{\sqrt{\pi}} \int_0^z e^{-\tau^2} d\tau \tag{6}$$

The values of the damping coefficients are related to the loss factor, η, which is a property of the material and is defined as the ratio of energy dissipated from the system to the energy stored in the system for every oscillation. The loss factor depends on a number of parameters, including the material composition, temperature, pre–strain level and frequency of deformation. The loss factor of neoprene has a value of 0.15 at room temperature, with no pre–strain and considering a deformation frequency of 1 Hz; loss factor grows considerably with frequency, reaching a value of 0.24 at 10 Hz [11]. The damping ratio, ζ, is proportional to the loss factor:

$$\zeta = \frac{\eta}{2} \tag{7}$$

which can be used to compute an equivalent damping coefficient:

$$c_j = \eta \sqrt{k_j m_j} \tag{8}$$

where the subscript j denotes a generic element of the vectors $\boldsymbol{c}$, $\boldsymbol{k}$ and $\boldsymbol{m}$.

Since the loss factor is not constant, the equivalent damping coefficients in Eq. 8 are, in general, not constant. Nevertheless, further approximation is introduced in the model by considering a constant loss factor value of 0.15, leading to the adoption of constant damping coefficients. This approximation is acceptable because in the considered case and experimental setup the temperature is constant, the first two natural frequencies of the system are generally limited below 10 Hz (depending on joint geometry) and pre–strain is small ($\varepsilon_r \leq 0.015$).

As a consequence of the axial symmetry of the damping joint, the deformation behaviour along some DoFs is equivalent and the following relations are valid:

$$\begin{aligned} k_x &\equiv k_y & k_\phi &\equiv k_\vartheta \\ c_x &\equiv c_y & c_\phi &\equiv c_\vartheta \end{aligned} \tag{9}$$

4. Numerical simulations

The design of the damping joint is supported by numerical simulations. Finite Element Method (FEM) simulations allow to estimate the rigidities of the damping joint and the influence of the main design parameters on them, providing design tools for the proper sizing of the damping joint. Dynamic simulations allow to estimate the forces transmitted by the joint to the support structure as the consequence of impacts.

4.1. Rigidity estimation

The estimation of the joint rigidity is performed by executing Modal Analysis FEM simulations in Solidworks Simulation. The simulations have been configured to resemble the laboratory set–up adopted during the experimental validation of the damping joint (see Sec. 5.1). In particular, three bodies are considered: (a) two deformable rubber elements and (b) a rigid body that replicates the inertial properties of a the 2 U CubeSat mock–up used in the experiments. The mass of the rigid body (b) is 2.293 kg (with uniform density) and its dimensions are shown in Fig. 4. The rubber disks are rigidly constrained at their external edges and connected to the CubeSat mock–up through a weld contact at their internal edges. The rubber disks are mounted on the cylindrical element that extends

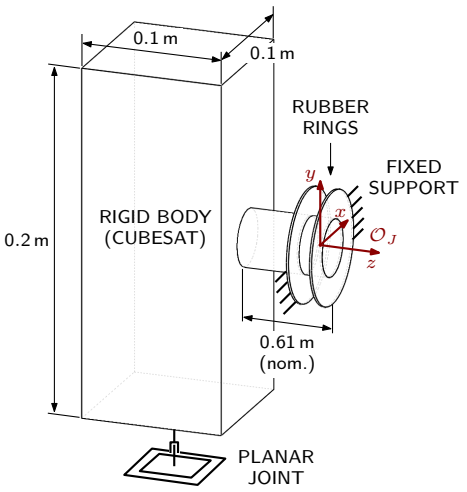

Figure 4: Simplified CAD model on which the FEM analyses have been conducted. Both rigid and deformable bodies are shown, as well as the main dimensions and the constraint conditions.

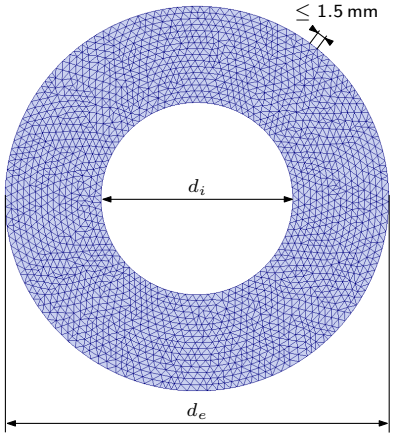

Figure 5: Graphic representation of the mesh of one rubber ring (nominal geometry); the elements are quadratic tetrahedrons.

from the side of the CubeSat and that emulates the docking mechanism. The only deformable bodies in this set–up are the rubber disks, whose deformation would allow 6 DoFs. The bottom side of the CubeSat is constrained to slide on the horizontal plane, to recreate a dynamic condition similar to that implemented in laboratory for the experimental validation (see Sec. 5). Hence, the number of DoFs allowed to the damping joint is limited to three, the translations along x and z, and the rotation (ϑ) around y in the joint frame of reference.

Linear FEM modal analyses have been conducted to compute the natural frequencies associated to the first three deformation modes shown in Fig. 6 and referred to as flexional (ϑ), axial (z) and radial (x). The third mode involves a rototranslation and does not imply a pure radial deformation of the joint. The main CubeSat body does not translate along the x axis, but rotates around a vertical axis parallel to y and passing through a point that is aligned with the center of mass (CM) along z, but located a few centimetres away from it in the $-z$ direction. The joint rigidities are computed from the natural frequencies (f_x, f_z, f_ϑ, in Hz) considering the mass, m and moments of inertia $I_y^{(CJ)}$ and $I_y^{(CR)}$, of the simplified CubeSat CAD model. Frequencies and rigidities are related by the following equations:

$$\begin{aligned} k_\vartheta &= (2\pi f_\vartheta)^2 I_y^{(CJ)} \\ k_z &= (2\pi f_z)^2 m \\ k_x &= (2\pi f_x)^2 \frac{I_y^{(CR)}}{a} \end{aligned} \tag{10}$$

where a is the distance between CR and CJ in Fig. 6. The values of $I_y^{(CJ)}$ and $I_y^{(CR)}$ are computed through the parallel axis theorem considering the moment of inertia at the center of mass and the distance between the y axis and its parallel y' passing through the joint center (CJ) or the center of rotation (CR) in the third mode. The value of a is variable and depending on the joint rigidity itself; for simplicity, the CR is assumed to be located approximately halfway between the CM and the back wall of the CubeSat.

The natural frequencies are strongly dependent on multiple parameters, including the geometry, the elastic properties of the material and the pre–stretch imposed to it. In order to understand the influence of these parameters on the joint natural frequencies and, hence, on its rigidities, multiple simulations have been conducted on models with different combinations of parameters. The considered parameters are the geometry (d_e, d_i, b and t from Fig. 2), the material hardness, H, and the radial pre–strain, ε_r.

Pre–stretching is a common technique to increase the rigidity of membranes. The two elastomeric elements can be pre–stretched radially to guarantee that the membranes remain planar and tight, with no wrinkles on the surface. The radial strain, ϵ_r, due to pre–stretch is computed by normalizing the length variation of the external radius, $\Delta_r = r_{e_f} - r_{e_i}$, by the value of the external diameter, d_e, of the membrane:

$$\epsilon_r = \frac{2\Delta_r}{d_e} \tag{11}$$

A nominal set of parameters is selected to define the baseline joint design adopted in the simulations and the values are reported in Tab. 1, along with the variability ranges considered for each parameter. Applying Eq. 5 to the nominal hardness value of 73 Sh A leads to an elastic modulus of 20.21 MPa. To obtain the maximum strain of 1.5 %, the radial deformation of the external edge of the rubber elements is $\Delta_r = 0.6$ mm.

Param.	d_e [mm]	d_i [mm]	b [mm]	t [mm]	H Sh A	ε_r [%]
Range	60 ÷ 90	30 ÷ 60	13.5 ÷ 19.5	1.5 ÷ 4.5	53 ÷ 73	0 ÷ 1.5
Nom.	80	40	16.5	1.5	73	0

Table 1: Ranges and nominal parameters considered during the modal analyses.

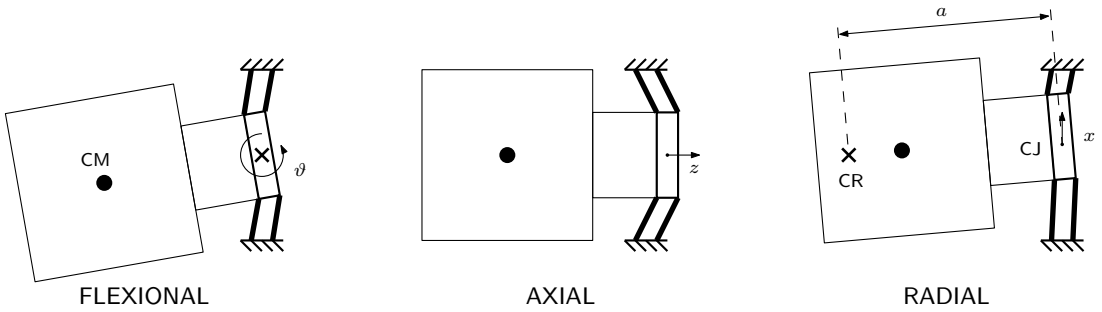

Figure 6: Simplified deformed representation of the three first vibration modes of the damping joint with a CubeSat docked to it.

The deformable bodies are meshed by quadratic tetrahedral elements (~ 29000 in the nominal design case) with a maximum side length of 1.5 mm (see Fig. 5). The rigid body is meshed only on its surface to implement the rigid contact with the deformable elastomeric bodies.

A total of 19 simulations has been executed with different combinations of parameters selected from the ranges listed in Tab. 1. In each simulation, only one parameter is modified form the nominal value, in order to determine the influence of that quantity on the natural frequencies and, consequently, on the joint rigidities. The values of joint rigidities are plotted in Fig. A1–A3 in the appendix.

Post–processing analysis has led to an empirical method that allows to estimate the joint rigidities of a particular joint design (i.e., combination of parameters). The rigidities of the nominal joint are the starting point for such estimation. Modifier coefficients are computed for each parameter that does not match the baseline configuration. These coefficients are computed through empirical relations obtained by fitting the simulation results. Assuming that the superimposition principle is valid, which is acceptable for small joint deformations, the nominal rigidities, $k_{\cdot_0}$, are multiplied by the coefficients, $\chi_{\cdot}^{(\cdot)}$, to obtain an estimate of the rigidity in the considered joint configuration. The values of the nominal rigidities and corresponding damping coefficients are:

$$\begin{aligned} k_{x_0} &= 14\,471\,\tfrac{\mathrm{N}}{\mathrm{m}} \quad & k_{z_0} &= 1573\,\tfrac{\mathrm{N}}{\mathrm{m}} \quad & k_{\vartheta_0} &= 9.361\,\tfrac{\mathrm{N\,m}}{\mathrm{rad}} \\ c_{x_0} &= 3.014\,\tfrac{\mathrm{N\,s}}{\mathrm{m}} \quad & c_{z_0} &= 6.756\,\tfrac{\mathrm{N\,s}}{\mathrm{m}} \quad & c_{\vartheta_0} &= 0.056\,\tfrac{\mathrm{N\,m\,s}}{\mathrm{rad}} \end{aligned} \tag{12}$$

Equation 13 presents the relations to compute the generic joint rigidities k_x, k_z and k_ϑ, while Eq. 14–16 list the empirical formulas to compute the modifier coefficients:

$$\begin{aligned} k_x &= k_{x_0}\chi_{d_e}^{(x)}\chi_{d_i}^{(x)}\chi_b^{(x)}\chi_t^{(x)}\chi_H^{(x)}\chi_{\varepsilon_r}^{(x)} \\ k_z &= k_{z_0}\chi_{d_e}^{(z)}\chi_{d_i}^{(z)}\chi_b^{(z)}\chi_t^{(z)}\chi_H^{(z)}\chi_{\varepsilon_r}^{(z)} \\ k_\vartheta &= k_{\vartheta_0}\chi_{d_e}^{(\vartheta)}\chi_{d_i}^{(\vartheta)}\chi_b^{(\vartheta)}\chi_t^{(\vartheta)}\chi_H^{(\vartheta)}\chi_{\varepsilon_r}^{(\vartheta)} \end{aligned} \tag{13}$$

$$\begin{aligned} \chi_{d_e}^{(x)} &= 5.298\times10^{-5}\,d_e^{-3.598} + 0.528 \\ \chi_{d_i}^{(x)} &= 0.262\,e^{33.3\,d_i} + 7.48\times10^{-6}\,e^{178.1\,d_i} \\ \chi_b^{(x)} &= 5.222\,b^{0.914} \\ \chi_t^{(x)} &= 668.7\,t \\ \chi_H^{(x)} &= 3.27\times10^{-7}\,H^{3.444} + 0.1465 \\ \chi_{\varepsilon_r}^{(x)} &= 4.922\,\varepsilon_r + 1 \end{aligned} \tag{14}$$

$$\begin{aligned} \chi_{d_e}^{(z)} &= 3.844^{-6}\,e^{-228.9\,d_e} + 108.1\,e^{-59.08\,d_e} \\ \chi_{d_i}^{(z)} &= 0.056\,e^{70.86\,d_i} + 4.341\times10^{-6}\,e^{235.9\,d_i} \\ \chi_b^{(z)} &= 1 \\ \chi_t^{(z)} &= 1.596\times10^{7}\,t^{2.523} - 0.1985 \\ \chi_H^{(z)} &= 3.438\times10^{-7}\,H^{3.432} + 0.145 \\ \chi_{\varepsilon_r}^{(z)} &= 346.7\,\varepsilon_r^{0.9688} + 1 \end{aligned} \tag{15}$$

$$\begin{aligned} \chi_{d_e}^{(\vartheta)} &= 4.062\times10^{-6}\,d_e^{-4.556} + 0.5945 \\ \chi_{d_i}^{(\vartheta)} &= 0.211\,e^{37.28\,d_i} + 1.137\times10^{-4}\,e^{158.2\,d_i} \\ \chi_b^{(\vartheta)} &= 2197\,b^{1.872} \\ \chi_t^{(\vartheta)} &= 1.688\times10^{4}\,t^{1.545} + 0.269 \\ \chi_H^{(\vartheta)} &= 1.167\times10^{-6}\,H^{3.157} + 0.110 \\ \chi_{\varepsilon_r}^{(\vartheta)} &= 19.35\,\varepsilon_r^{0.9073} + 1 \end{aligned} \tag{16}$$

4.1.1. 6–DoF simulation

A single 6–DoF simulation has been conducted in order to assess the possible differences in joint rigidities in comparison to the simplified planar case. As already mentioned, the joint deformations along different DoFs are coupled and the system dynamic behaviour is influenced by this. In the planar case the constraints limit the motion of the system thus reducing the effects of mechanical coupling. The goal of the 6–DoF simulation is to quantify the differences in joint rigidities between the laboratory case and an hypothetical free–floating scenario. The nominal

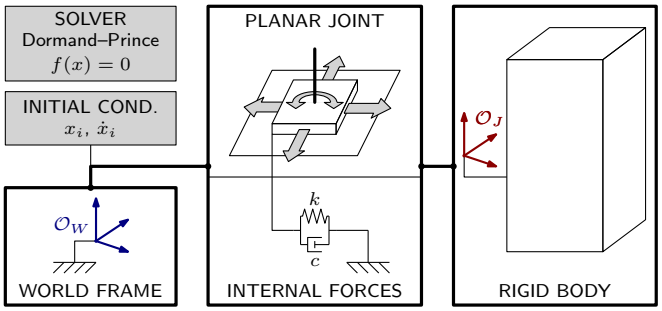

Figure 7: Simplified representation of the Simulink Simscape model used to execute the dynamic simulations.

joint design is considered and the rigidities in this case are:

$$k_{x_{3D}} = 16\,028\ \frac{\mathrm{N}}{\mathrm{m}} \quad k_{y_{3D}} = 19\,724\ \frac{\mathrm{N}}{\mathrm{m}} \quad k_{z_{3D}} = 1574\ \frac{\mathrm{N}}{\mathrm{m}}$$
$$k_{\phi_{3D}} = 9.501\ \frac{\mathrm{N\,m}}{\mathrm{rad}} \quad k_{\theta_{3D}} = 9.472\ \frac{\mathrm{N\,m}}{\mathrm{rad}} \quad k_{\psi_{3D}} = 40.12\ \frac{\mathrm{N\,m}}{\mathrm{rad}} \tag{17}$$

The values of $k_{x_{3D}}$, $k_{z_{3D}}$, $k_{\phi_{3D}}$ and $k_{\theta_{3D}}$ are similar to the respective values of k_{x_0}, k_{z_0}, k_{ϕ_0} and k_{θ_0}, with differences below 10%. Considered this limitation, the experimental verification of the damping joint behaviour in a simplified planar condition is valid also for a free–floating scenario. Note the $\sim$ 20% difference between $k_{x_{3D}}$ and $k_{y_{3D}}$, which is in contrast with the assumption in Eq. 9. This is due to the uncertainty in the determination of the value of a (see Eq. 10).

4.2. Dynamic simulations

A number of dynamic simulations have been executed implementing the simplified dynamic model of the damping joint to evaluate the behaviour of the system numerically. The main goal of the simulations is to validate the dynamic model through comparison with the experimental results. The geometric configuration of the experiments is planar and, for consistency, the dynamic simulations implement a planar scenario as well. In particular, if a docking manoeuvre is considered, the simulation recreates down–scaled version of a scenario where a nanosatellite chaser (2 U CubeSat) connects to a much larger target vehicle. The target, due to its large mass and inertial properties, does not move as a consequence of the manoeuvre and is simulated by a fixed world frame, $\mathcal{O}_\mathcal{J}$. The simulation starts immediately after a rigid connection is established between the chaser and the target.

The simulations have been implemented in the MATLAB/Simulink Simscape environment, which allows to easily implement multibody dynamic simulations through a graphical interface based on block diagrams. The dynamic model implemented is composed by a single rigid body resembling the inertial properties of a 2 U CubeSat, which is connected to the static world frame $\mathcal{O}_W$ through a planar joint that allows three DoFs. Concerning rigid body geometry, the simulation model resembles the model adopted for the FEM analysis and shown in Fig. 4. Internal forces are

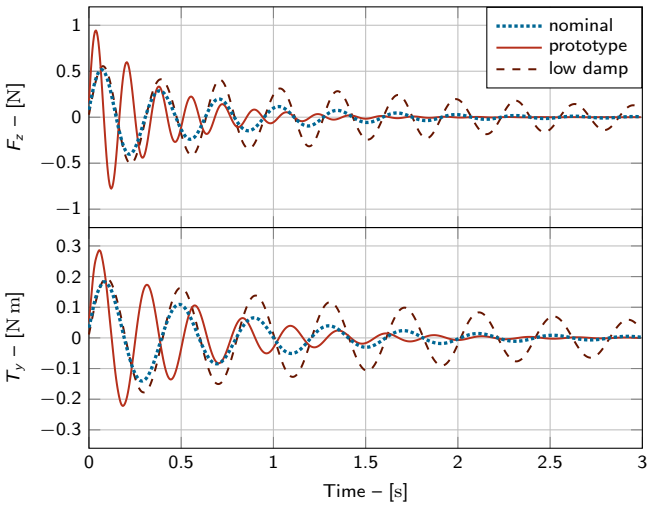

Figure 8: Force and torque comparison between two different joint designs (the nominal design and the design implemented in the laboratory prototype) and the low–damped version of the nominal design.

defined in the joint in order to simulate the visco–elastic reactions of the damping joint. The simulation configuration is completed by setting numerical solver (Runge–Kutta Dormand–Prince method, maximum step size 1 ms) and by the defining the initial conditions on the joint velocities (joint initial positions are null):

$$\dot{x}_{IC} = 5\,\mathrm{mm/s} \quad \dot{z}_{IC} = 12\,\mathrm{mm/s} \quad \dot{\vartheta}_{IC} = 23\,\mathrm{deg/s} \tag{18}$$

Figure 7 is a simplified representation of the Simscape block diagram developed.

In order to compare the behaviour of the system when different joint designs are implemented, two joint configurations are considered: the nominal design and the laboratory prototype design. The values of rigidity and damping coefficients in the nominal design, $k_{\cdot_0}$ and $c_{\cdot_0}$, are reported in Eq. 12, while the values in the prototype configuration, $k_{\cdot_P}$ and $c_{\cdot_P}$, are:

$$k_{x_P} = 16\,570\ \frac{\mathrm{N}}{\mathrm{m}} \quad k_{z_P} = 3211\ \frac{\mathrm{N}}{\mathrm{m}} \quad k_{\vartheta_P} = 15.42\ \frac{\mathrm{N\,m}}{\mathrm{rad}}$$
$$c_{x_P} = 4.054\ \frac{\mathrm{N\,s}}{\mathrm{m}} \quad c_{z_P} = 12.87\ \frac{\mathrm{N\,s}}{\mathrm{m}} \quad c_{\vartheta_P} = 0.097\ \frac{\mathrm{N\,m\,s}}{\mathrm{rad}} \tag{19}$$

The time evolution of dynamic loads is the most relevant result of the simulations, highlighting the advantages of including a damping joint in the docking system. Figure 8 presents the results comparison between the two considered designs in terms of simulated axial force, F_z, and torque around the vertical axis, T_y. The prototype joint configuration is stiffer compared to the nominal design and this reflects in higher oscillation frequencies and maximum peak loads for both force and torque. This result confirms that the rigidity of the connection between the two satellites influences the peak loads and their oscillation frequency, thus proving that introducing a flexible joint is advantageous.

The deformable joint enhances the oscillation damping performance compared to the case in which a rigid connection is adopted. The oscillation damping is due to internal dissipation of energy in the materials involved, which is quantified by the loss factor η. The adoption of elastomeric deformable elements reduces the time to attenuate the oscillations thanks to the relatively high value of η. This is shown through a third simulation in which a reduced value of $\eta = 0.05$ is adopted. The dashed lines in Fig. 8 follow the evolution of loads in the third low–damped case. These results prove that a highly dissipating material is required to obtain a faster damping of the oscillations, thus confirming the advantage of using elastomers compared to more rigid structural materials.

5. Experimental validation

An extensive experimental campaign has been conducted on a damping joint prototype, aiming at proving the advantages provided by the adoption of the compliant joint in a docking application. In particular, the objectives of the testing activity are:

1. the validation of the equivalent dynamic model (i.e., rigidities and damping coefficients) presetned in Sec. 3;
2. the quantification of the joint dynamic performance (i.e., loads reduction and energy dissipation).

The design parameters of the tested prototype (Fig. 1) are summarized in Tab. 2. The rubber elements are manufactured from a neoprene sheet (mass density 1350 kg/m^3), whose hardness has been measured in laboratory (durometer Sauter HBA 100-0).

Param.	d_e [mm]	d_i [mm]	b [mm]	t [mm]	H Sh A	ε_r [%]
Value	80	40	20.5	1.5	73	0.25

Table 2: Design parameters implemented in the joint prototype.

5.1. Test setup

The experimental estimation of the joint performance and the validation of the numerical models is conducted in a simplified planar configuration, allowing a total of three DoFs (translations along x and z, rotation around y). The experimental setup is a down–scaled laboratory replica of a close–proximity scenario in which a nanosatellite approaches and docks to a much larger mother ship, which is represented in laboratory by a fixed docking interface. Exploiting the equivalences in Eq. 9, the simplified experiment allows to validate the dynamic parameters relative to five DoFs (x, y, z, ϕ, ϑ). The dynamics of the rotation around the z–axis is not validated experimentally.

Figure 9 depicts the experimental setup. A flat table ($\sim 1\,\mathrm{m}^2$), composed by a glass plate laid on an optical breadboard (Thorlabs B90120B), is the low–friction

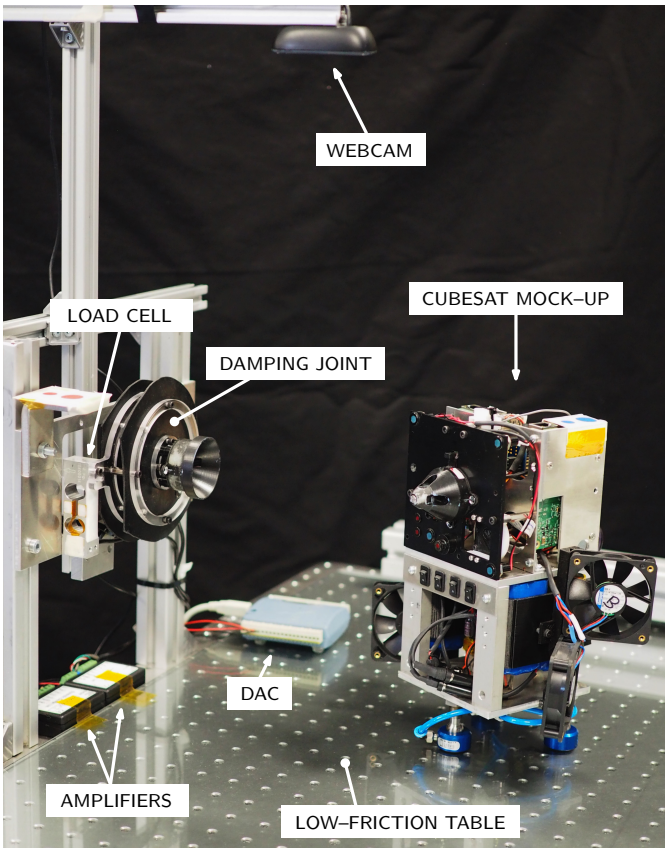

Figure 9: The test setup employed for the experimental validation of the damping joint.

environment that allows to execute dynamic testing with minimum influence from external loads. A 2 U–CubeSat mock–up is employed to replicate the inertial properties and emulate the dynamics of a nanosatellite that docks to a larger orbital vehicle. The vehicle stands on air bearings (New Way Air Bearings S102501) that guarantee a virtually frictionless motion on the plane (residual friction coefficient is in the order of 10^{-6}). The floating module is the same used in [5]. The vehicle mass is 2.3 kg and its structure resembles a tall parallelepiped (10 cm × 10 cm × 20 cm) with a square basis.

The relative trajectory between the floating mock–up and the target structure is monitored by a vision system based on a webcam (Logitech C270 HD, frame rate: 10 fps) that observes the scene from above. The camera reconstructs the relative position and orientation of two optical markers, one mounted on the floating vehicle, the other fixed in the laboratory frame of reference.

The damping joint under test is mounted on a structure fixed to the optical breadboard. The supporting structure is equipped with two load cells that sense the forces along the $\pm z$ direction (sensors: Tedea–Huntleigh Mod. 1006, amplifiers: Synectic Design SY011 V100–10–2, acquisition: Measurement Computing USB–1408FS–Plus). The rigid element A of the damping joint (see Fig. 3) is directly connected to the load cells, while the rigid element

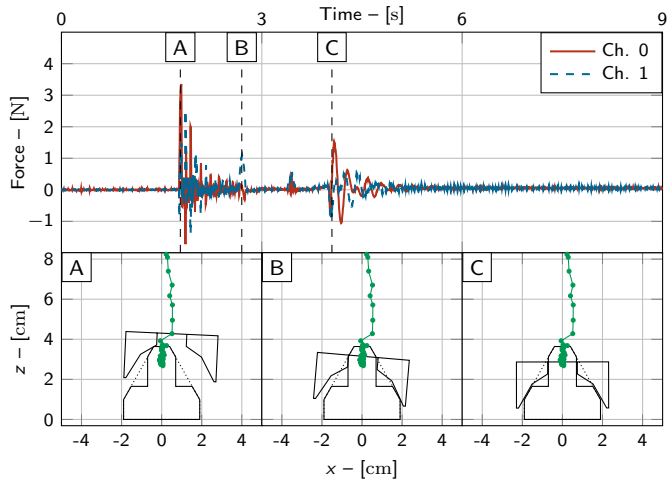

(a) Smooth docking. Misalignments at first contact: $\Delta x = 5.2\,\text{mm}$ and $\Delta\vartheta = -2.7\,\text{deg}$.

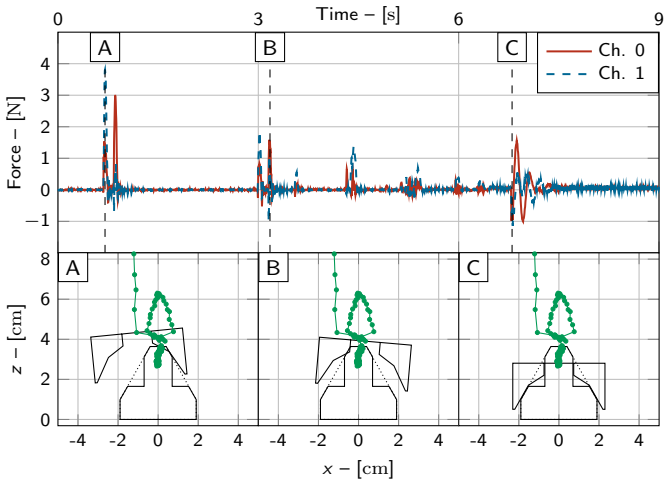

(b) Rough docking. Misalignments at first contact: $\Delta x = 10.2\,\text{mm}$ and $\Delta\vartheta = 4.1\,\text{deg}$.

Figure 10: Data retrieved from two example docking tests. The top plots represent the forces measured by the two load cells (channel 0 and channel 1); the bottom images report the final path with three snapshots of the relative pose between the two docking interfaces (probe and drogue).

B holds the docking interface. The distance between the two load cells is $b_{LC} = 138\,\text{mm}$ and the torque around the vertical axis y can be estimated by computing the difference between the two measured forces, F_{Ch0} and F_{Ch1}. The total measured force, F_z, and torque, T_y, are computed with the following relations:

$$\begin{aligned} F_z &= F_{Ch0} + F_{Ch1} \\ T_y &= \frac{b_{LC}}{2}(F_{Ch0} - F_{Ch1}) \end{aligned} \tag{20}$$

The docking mechanism adopted is the probe–drogue system described in [5], whose geometry tolerates misalignments greater than $\pm 20\,\text{mm}$ along the x axis and $\pm 5\,\text{deg}$ for θ. The active drogue is mounted on the floating vehicle, while the passive drogue is mounted on a fixed structure through the damping joint. The drogue features a hard–docking actuator that locks the connection with the probe after full connection is achieved and acknowledged.

A set of fans (epm-pabst 605F–RS0) provides a constant thrust that accelerates the vehicle towards the fixed structure holding the docking drogue. The total measured force generated by the fans is 76 mN.

5.2. Test results

At the beginning of each test run the floating vehicle stands a few centimetres away from the target structure, approximately along the z direction of the joint reference frame $\mathcal{O}_J$. The fans are activated, the vehicle is released and accelerates until the two docking interfaces get in contact. The data collected are the relative state $\{x, y, \vartheta\}$ between chaser and target, and the impact force signals from the load cells (Ch. 0 and Ch. 1). The relative velocities are estimated from the position signals through numerical differentiation. The vehicle trajectory is uncontrolled and, therefore, each test run differs from the others in terms of misalignments and velocities at contact. The behaviour of the system during the docking procedure is influenced by the specific test condition, with the dynamic evolution of the system that can vary from a smooth insertion of the probe into the drogue with a single contact that leads to a safe hard–docking, to a multiple–contact manoeuvre that may lead to rebounds and unsuccessful docking. Figure 10 presents the measured forces and the vehicle trajectory in two different cases:

I. Smooth docking (Fig. 10a): after a first contact (A), the probe slides into the droque exchanging forces with it (B), until the full contact is achieved and the latching mechanism is activated (C). Misalignments at first contact are $\Delta x = 5.2\,\text{mm}$ and $\Delta\vartheta = -2.7\,\text{deg}$.

II. Rough docking (Fig. 10b): the first contact (A) is strong and causes the vehicle to bounce back; the second contact (B) is the first of a number of contacts that finally lead to the full insertion of the probe and the latching mechanism activation (C). Misalignments at first contact are $\Delta x = 10.2\,\text{mm}$ and $\Delta\vartheta = 4.1\,\text{deg}$.

Experimental results show that, due to the adoption of the probe–drogue configuration, the dynamic evolution of the docking manoeuvre very often begins with a double contact between the tip of the probe and the internal surfaces of the drogue. Further double contacts may happen until the relative velocities are reasonably dumped and the probe can slide inside the drogue under the effect of the fan thrust. When full insertion is achieved, the docking latch

Table 3: Dynamic experimental results: comparison between flexible (with joint) and rigid (without joint) test configurations.

Quantity		No joint avg.	No joint std.†	With joint avg.	With joint std.†	Diff.
f_ϑ	[Hz]	7.23	1.93	4.00	0.23	-45%
f_z		17.96	1.62	6.01	0.14	-67%
k_{ϑ_P}	$\left[\frac{\mathrm{N\,m}}{\mathrm{rad}}\right]$	41.93	11.18	12.88	0.75	-69%
k_{z_P}	$\left[\frac{\mathrm{N}}{\mathrm{m}}\right]$	29206	2637	3265	77	-89%
$\hat{F}_{z_i}$	$\left[\frac{\mathrm{N\,s}}{\mathrm{m}}\right]$	1.54	0.71	0.60	0.23	-61%
$\hat{F}_{z_{max}}$		2.03	0.46	0.75	0.21	-63%
$\hat{T}_{y_i}$	[mN s]	60.4	18.3	23.3	8.7	-61%
$\hat{T}_{y_{max}}$		115.3	25.5	61.6	30.9	-47%
$t_{50\%}$	[s]	0.211	0.137	0.186	0.113	-12%
$t_{10\%}$		1.093	0.779	0.770	0.273	-26%

† For k_{ϑ_P} and k_{z_P} the std is propagated from f_ϑ and f_z.

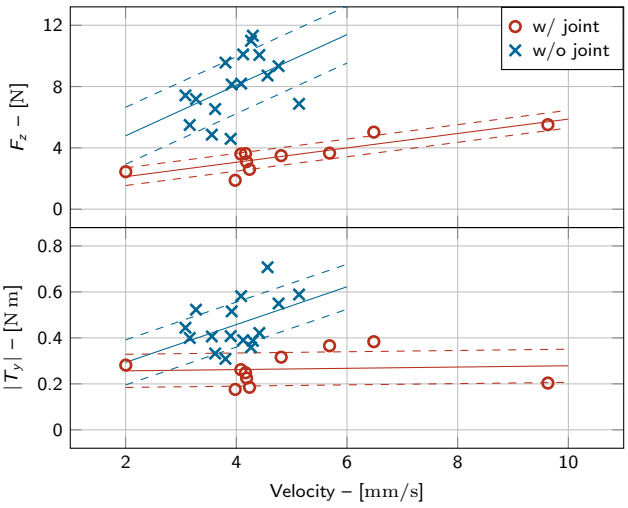

Figure 11: Dependence of maximum loads on impact velocity with and without damping joint.

is activated, generating a rigid connection between the two interfaces (hard docking). The after–docking residual misalignments and relative velocities transmit loads to the system structures, leading to oscillations in the damping joint at the natural frequencies. The damping joint design and dynamic model are validated by studying these oscillations.

In order to estimate the performance of the damping joint, a rigid configuration of the test setup is assembled and used for comparison: the compliant joint is replaced by a rigid structure with the same geometry and dimensions of the joint. The rigid structure is an assembly of polycarbonate components machined from 5 mm thick sheets and held together with metal standoffs. As reported in Tab. 3, the polycarbonate supports are three times more rigid in the z translation and nine times more rigid if the rotation around y is considered.

The comparison between the data collected through experiments in the two configurations (with damping joint and rigid) shows how the damping joint reduces the loads exchanged between the two docking interfaces at contact. The contact dynamics is complex and depend strongly on the momentum of the objects involved in the impact. In the proposed experimental setup, the momentum, $p = mv$, is carried entirely by the chaser mock–up, whose mass is constant regardless of the experiment configuration considered. The contact generates an initial peak of loads whose intensity and duration depend on the momentum of the impactor. Figure 11 presents the relation between the maximum docking loads and the velocity at contact (proportional to the momentum), showing how the values of maximum loads are strongly dependent on the velocity. In addition, the adoption of the damping joint reduces the loads considerably, although this advantage is greatly reduced at low contact velocities.

In order to guarantee a fair comparison between test runs characterized by different impact velocities, the loads at first contact are normalized dividing them by the chaser velocity:

$$\hat{F}_{z_i} = \frac{F_{z_i}}{v_i} \qquad \hat{F}_{z_{max}} = \frac{F_{z_{max}}}{v_i}$$
$$\hat{T}_{y_i} = \frac{|T_{y_i}|}{v_i} \qquad \hat{T}_{y_{max}} = \frac{|T_{y_{max}}|}{v_i} \tag{21}$$

Table 3 presents the results of the comparison between the two test configurations. Besides the estimated values of oscillation frequencies and rigidities in flexional and axial modes, the table presents the mean values and standard deviations of the exchanged loads (normalized), as well as the time required to damp the oscillations to 50% and 10% of the initial value, $t_{50\%}$ and $t_{10\%}$ respectively. The adoption of the damping joint proves advantageous, reducing frequencies, rigidities, loads and damping time. The percentage reduction is also reported.

In order to validate the joint visco–elastic equivalent model, the loads resulting from dynamic simulations are compared with the loads measured during the experiments in Fig. 12, showing a good accordance between experimental and numerical results. The values of oscillation frequencies in the simulated and experimental cases is very similar ($< 10\%$ difference in the torque case), proving that Eq. 13 provides good estimates. In addition, the equivalent viscous damping model is accurate in simulating the attenuation of oscillations over time.

6. Conclusions

The docking between small satellites to enable a large variety of advanced mission operations is an appealing concept that is close to become reality, motivating the development of critical technologies like docking mechanisms and systems. Although several examples of miniature docking mechanisms are available in the literature, the problem of exchanged loads and their management is

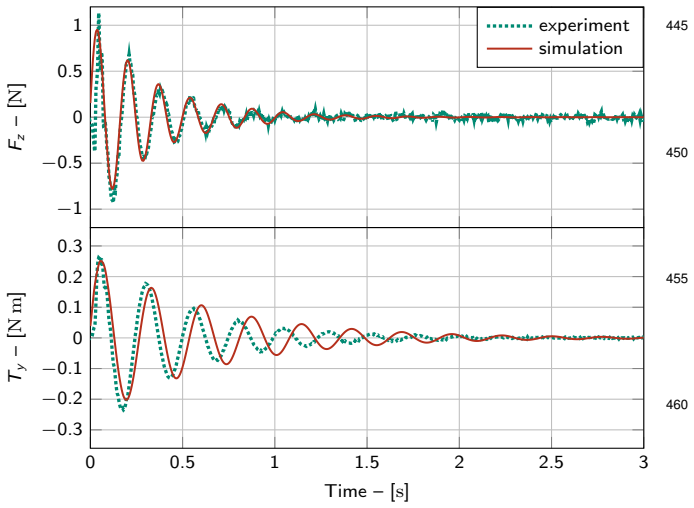

Figure 12: Force and torque comparison between simulation and experimental results.

rarely discussed in available studies. This work suggests the use of a passive damping joint to reduce the rigidity of contact and the docking loads, while efficiently dissipating any residual motion. Although a specific design is proposed, for which sizing relations are provided, the obtained results have a general relevance since they prove the advantages of implementing some sort of passively damping device in the docking system.

More in detail, the adoption of the damping joint reduces the natural frequencies and rigidities of the contact dynamics, the initial and maximum loads (forces and torques), and the time to attenuate oscillations to a fraction of the initial displacements. The actual percentage reduction of the mentioned quantities ranges between 12% and 89% in the tested cases, but is strongly dependent on the joint geometry and inertial characteristics of the system. Maximum loads are a function of the system relative momentum at the time of contact, resulting in a strong dependence of forces and torques on the initial velocity.

The proposed design is described in detail and the influence of the most relevant design parameters is taken into account while evaluating the joint mechanical properties (rigidity and damping coefficient). Parametric relations are presented to provide the reader with a tool to estimate the joint properties, resulting in an equivalent visco–elastic model of the joint dynamics. Results from simulations and experiments are compared in order to validate the developed model and assess the joint performance.

References

[1] A. Golkar, A. Salado, Definition of New Space—Expert Survey Results and Key Technology Trends, IEEE Journal on Miniaturization for Air and Space Systems 2 (1) (2021) 2–9. doi:10.1109/JMASS.2020.3045851.

[2] A. Nanjangud, P. Blacker, S. Bandyopadhyay, Y. Gao, Robotics and AI-enabled on-orbit operations with future generation of small satellites, Proceedings of the IEEE 106 (3) (2018) 429–439.

[3] P. Tchoryk Jr, A. B. Hays, J. C. Pavlich, A docking solution for on-orbit satellite servicing: part of the responsive space equation, AIAA-LA Section/SSTC 2001 (2003) 1–3.

[4] A. Boesso, A. Francesconi, ARCADE small–scale docking mechanism for micro-satellites, Acta Astronautica 86 (2013) 77–87.

[5] F. Branz, L. Olivieri, F. Sansone, A. Francesconi, Miniature docking mechanism for CubeSats, Acta Astronautica 176 (2020) 510–519. doi:https://doi.org/10.1016/j.actaastro.2020.06.042.

[6] L. Rodgers, N. Hoff, E. Jordan, M. Heiman, D. Miller, A universal interface for modular spacecraft, in: 19th Annual AIAA/USU Conference on Small Satellites, 2005.

[7] C. S. Pirat, P.-A. Mäusli, R. Walker, F. Ankersen, V. Gass, Guidance, Navigation and Control for Autonomous Cooperative Docking of CubeSats, 2018, p. 15.
URL http://infoscience.epfl.ch/record/255877

[8] J. Bowen, A. Tsuda, J. Abel, M. Villa, CubeSat Proximity Operations Demonstration (CPOD) mission update, in: 2015 IEEE Aerospace Conference, 2015, pp. 1–8. doi:10.1109/AERO.2015.7119124.

[9] L. Olivieri, A. Francesconi, Design and test of a semiandrogynous docking mechanism for small satellites, Acta Astronautica 122 (2016) 219–230.

[10] C. Underwood, S. Pellegrino, V. J. Lappas, C. P. Bridges, J. Baker, Using CubeSat/micro-satellite technology to demonstrate the Autonomous Assembly of a Reconfigurable Space Telescope (AAReST), Acta Astronautica 114 (2015) 112 – 122.

[11] M. Febbo, E. M. O. Lopes, C. A. Bavastri, Influence of temperature on optimum viscoelastic absorbers in cubic nonlinear systems, Journal of Vibration and Control 22 (15) (2016) 3396–3412. doi:https://doi.org/10.1177/1077546314560202.

Appendix

The numerical results of the FEM Modal Analysis are reported here in the form of plots of joint rigidities as a function of the six design parameters considered.

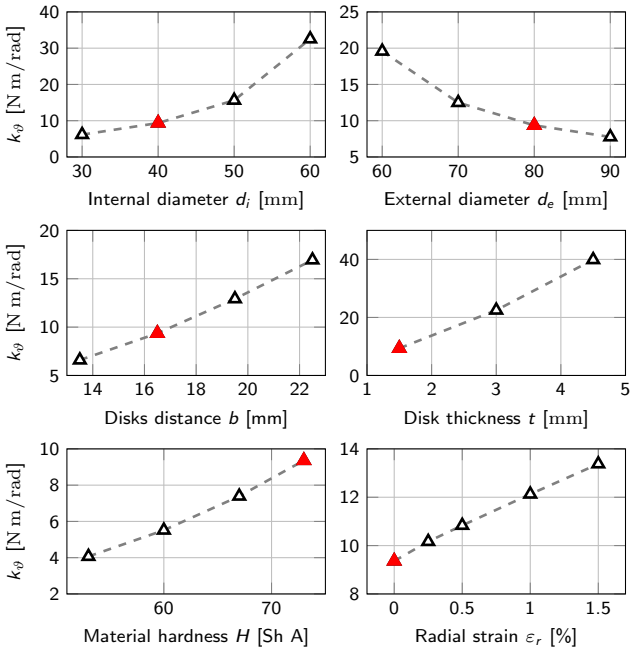

Figure A1: Influence of the design parameters on k_ϑ; the red triangle corresponds to the nominal design configuration.

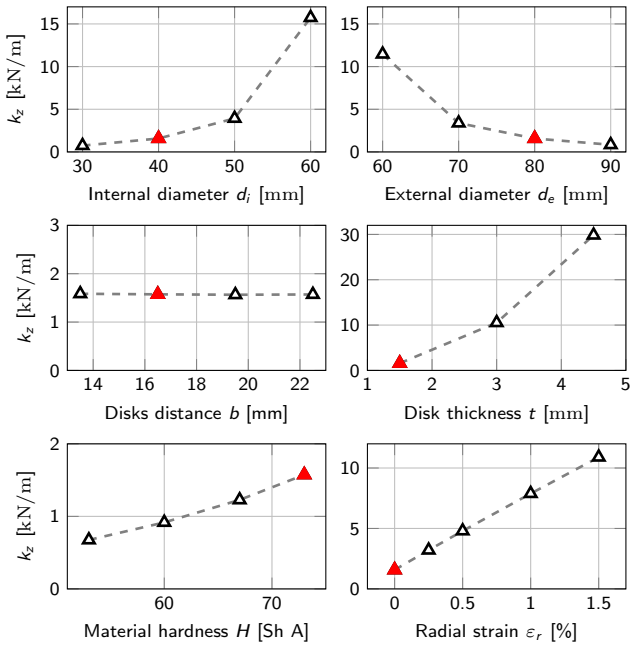

Figure A2: Influence of the design parameters on k_z; the red triangle corresponds to the nominal design configuration.

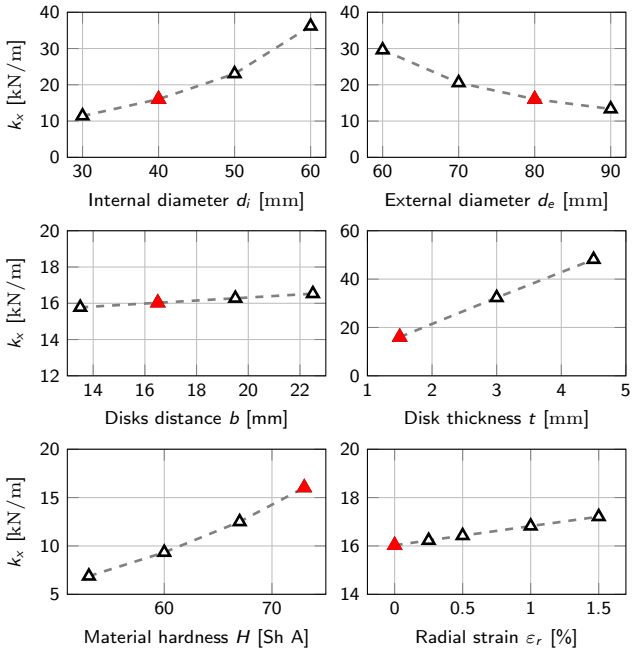

Figure A3: Influence of the design parameters on k_x; the red triangle corresponds to the nominal design configuration.

Biographies

Francesco Branz is a research associate in Space Systems and Equipments with the Dept. of Industrial Engineering of the University of Padova. His research interests focus on space robotics, CubeSat technology, relative navigation sensors, docking mechanisms, and optical communication. He has taken part in several national and international research projects. Recently, he has been technical leader in two ESA–funded projects: the development of a CubeSat–sized docking mechanism in the framework of the Space Rider Observer Cube (SROC) mission, and the development of a simulation tool for the validation of GNC algorithms to enable the capture of space vehicles by a manipulator–equipped chaser satellite.

Alessandro Francesconi is associate professor of Space Systems at University of Padova. His main research topics are related to spacecraft systems and miniature satellites (with focus on on–orbit servicing, docking and capture of non–cooperative spacecraft, and laser communication), and space debris (where he has 20+ years of experience in studying hypervelocity impacts, satellites collisions and fragmentation). He has been chairman of the Protection Working Group of the Inter Agency Debris Coordination Committee, and he is member of the IAA Permanent Committee on Space Debris.